THE JOURNAL OF PHYSICAL CHEMISTRY C

Article

pubs.acs.org/JPCC

Measuring Protein Binding to Individual Hydrogel Nanoparticles with Single-Nanoparticle Surface Plasmon Resonance Imaging Microscopy

Adam M. Maley,[§,†] Yuhei Terada,[§,‡] Shunsuke Onogi,[†] Kenneth J. Shea,[†] Yoshiko Miura,[*,‡] and Robert M. Corn[*,†]

[†]Department of Chemistry, University of California—Irvine, Irvine, California 92697, United States

[‡]Department of Chemical Engineering, Graduate School of Engineering, Kyushu University, 744 Motooka, Nishi-ku, Fukuoka 819-0395, Japan

Supporting Information

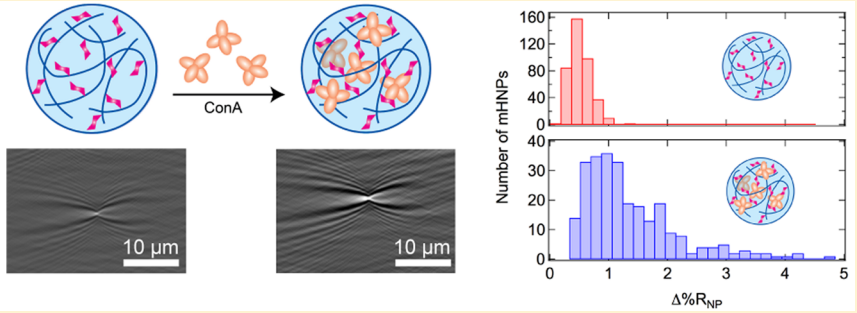

ABSTRACT: The specific binding and uptake of protein molecules to individual hydrogel nanoparticles is measured with real-time single-nanoparticle surface plasmon resonance imaging (SPRI) microscopy. Nanoparticles that adsorb onto chemically modified gold thin films interact with traveling surface plasmon polaritons and create individual point diffraction patterns in the SPRI microscopy differential reflectivity images. The intensity of each point diffraction pattern depends on the integrated refractive index of the nanoparticle; an increase in this single nanoparticle point diffraction intensity ($\Delta\%R_{NP}$) is observed for nanoparticles that bind proteins. SPRI adsorption measurements can be used to measure an average increase in $\Delta\%R_{NP}$ that can be correlated with bulk dynamic light scattering measurements. Moreover, the distribution of $\Delta\%R_{NP}$ values observed for individual nanoparticles can be used to learn more about the nature of the protein−nanoparticle interaction. As a first example, the binding of the lectin Concanavalin A to 180 nm *N*-Isopropylacrylamide hydrogel nanoparticles that incorporate a small percentage of mannose sugar monomer units is characterized.

INTRODUCTION

Hydrogel nanoparticles (HNPs) are unique synthetic nanomaterials that can incorporate various chemical functionalities specifically designed to capture and release proteins, peptides, or other small molecules. These capabilities have led to a significant interest in the potential use of HNPs in biomedical applications such as targeted drug delivery, medical diagnostics, and biosensing.[1−6] For example, NIPAm-based (*N*-Isopropylacrylamide) HNPs have been utilized for detection of various biomolecules, such as DNA,[7,8] proteins,[9−11] and other biologically relevant small molecules.[12,13] Additionally, the specific uptake of proteins into HNPs can also be used as a model system for studying various biological phenomena such as multivalent lectin−carbohydrate interactions.[14−20] For all of these applications, it is essential that the uptake of proteins into individual nanoparticles be quantitated and analyzed. For the case of fluorescently labeled proteins, single nanoparticle fluorescence imaging can be used to monitor affinity uptake into single HNPs.[21−23] For nonfluorescent proteins, the average particle size and molecular weight of HNPs can be obtained by a combination of dynamic light scattering (DLS)[24,25] and multiangle light scattering (MALS),[26] but measurements of single HNPs are more difficult, typically requiring methods such as cryo-TEM or atomic force microscopy.[27−29]

Recently, we have demonstrated that real-time single-nanoparticle surface plasmon resonance imaging (SPRI) microscopy can be used to detect single HNPs *in situ* and quantitatively monitor the specific uptake of nonfluorescent biomolecules into the individual nanoparticles.[30] SPRI microscopy has been used previously to study single metallic nanoparticles, membrane proteins, cells, and viruses;[31−42] an example of the SPRI microscopy experimental setup is shown in Figure 1a. When a nanoparticle adsorbs onto a chemically

Received: June 6, 2016
Revised: July 8, 2016
Published: July 11, 2016

DOI: 10.1021/acs.jpcc.6b05700
J. Phys. Chem. C 2016, 120, 16843−16849

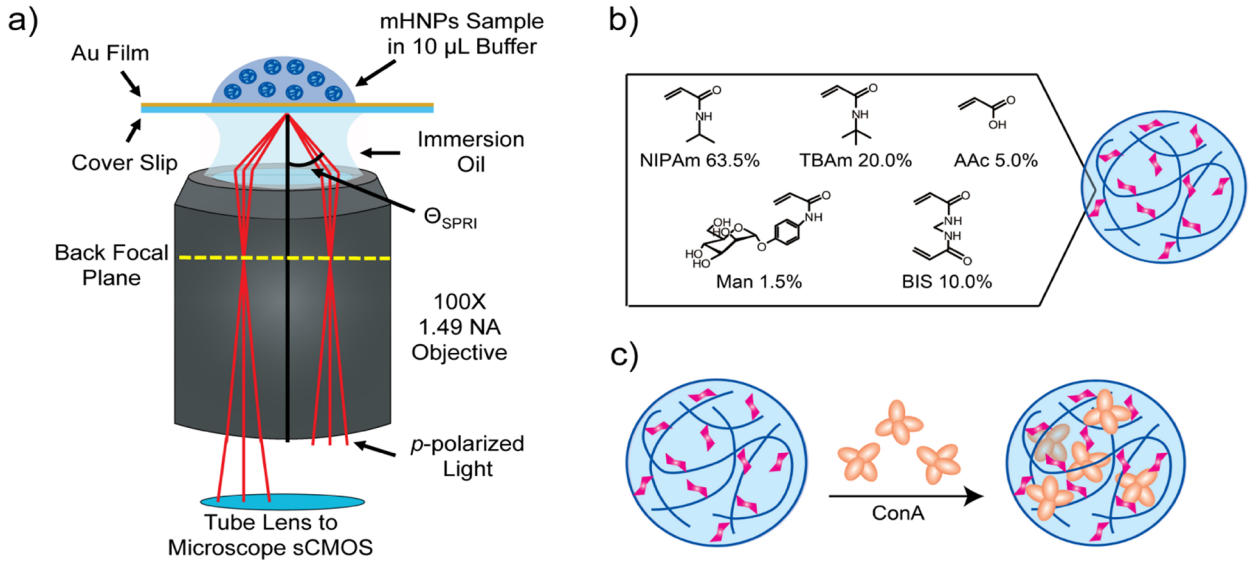

Figure 1. (a) Schematic diagram of the SPRI microscope. A knife-edge mirror was used to send collimated *p*-polarized light through the objective at the SPRI angle of 30% reflectivity. The reflected images were collected by the sCMOS camera. (b) Mannose-incorporated hydrogel nanoparticles (mHNPs) were synthesized from *N*-Isopropylacrylamide (NIPAm, 63.5 mol %), *N-tert*-Butylacrylamide (TBAm, 20 mol %), acrylic acid (AAc, 5 mol %), *N*,*N*′-Methylenebis(acrylamide) (BIS, 10 mol %), and *p*-acrylamidophenyl-α-D-mannopyranoside (Man, 1.5 mol %). (c) The uptake of Concanavalin A (Con A) into mHNPs was monitored by SPRI microscopy. Con A specifically binds to mannose sugar units (pink) in the mHNPs.

modified gold thin film from solution, a large point diffraction pattern in the SPRI microscopy image is created from the interaction between the nanoparticle and the traveling surface plasmon polaritons. This single-nanoparticle point diffraction intensity can be quantitated and is expressed as a change in percent reflectivity ($\Delta\%R_{NP}$).[30,41] The value of $\Delta\%R_{NP}$ for a single nanoparticle depends on its integrated refractive index and thus, in the case of HNPs, on the amount of protein adsorbed and incorporated to the nanoparticle. In our recent paper, we synthesized NIPAm-based HNPs with specific affinity for the peptide melittin.[30] SPRI microscopy was then used to quantify the average uptake of melittin into these HNPs by calculating average $\Delta\%R_{NP}$ values from individual HNPs. We showed that although the average HNP size (as measured by DLS) did not change with melittin concentration the average $\Delta\%R_{NP}$ varied linearly due to melittin uptake into the HNPs.

In this paper, we extend our use of single-nanoparticle SPRI microscopy to monitor the specific adsorption and uptake of proteins to individual HNPs. We have synthesized NIPAm-based HNPs that incorporate a small percentage of monomers modified with mannose sugar units into the hydrogel polymer as shown in Figure 1b. We then used SPRI microscopy to monitor the interactions of the lectin Concanavalin A (Con A) to these mannose-incorporated HNPs (mHNPs), shown in Figure 1c. Both the average and distribution of $\Delta\%R_{NP}$ values for single mHNPs in the presence of Con A were quantitated; an increase in the average $\Delta\%R_{NP}$ due to the combination of Con A binding to the mHNPs and Con A-induced specific aggregation of mHNPs was observed for solutions up to 200 nM. We also found that the interaction of Con A with the mHNPs led to a significant increase in the distribution of $\Delta\%R_{NP}$ values that we attribute to variations of mannose sugar unit availability for Con A binding in individual mHNPs. At Con A concentrations above 200 nM, a saturation of binding and mHNP aggregation led to an observed leveling off of the $\Delta\%R_{NP}$ values for the single mHNPs.

EXPERIMENTAL METHODS

Hydrogel Nanoparticle Materials. NIPAm, acrylic acid (AAc), sodium dodecyl sulfate (SDS), and V-501 were obtained from Sigma-Aldrich, Inc. (St. Louis, MO). *N*,*N*′-Methylenebis(acrylamide) (BIS) was obtained from Fluka (St. Louis, MO). *N-tert*-Butylacrylamide (TBAm) was obtained from Acros Organics (Geel, Belgium). NIPAm was recrystallized from hexane before use. All other chemicals were used as received.

Hydrogel Nanoparticle Synthesis. The sugar unit *p*-acrylamidophenyl-α-D-mannopyranoside (Man) was synthesized using methods reported previously.[24,43] mHNP synthesis was adapted from previous HNP synthesis methods.[44,45] The monomers NIPAm (63.5 mol %), TBAm (20 mol %), AAc (5 mol %), BIS (10 mol %), and Man (1.5 mol %) and 2.5 mg (8.7 μmol) of SDS were dissolved in 50 mL of nanopure water for a total monomer concentration of 65 mM. TBAm was dissolved in 1 mL of ethanol before addition to nanopure water. Nitrogen gas was bubbled through the mixture for 30 min. Following the addition of V-501 (131.3 μmol/0.5 mL of DMSO), the polymerization was carried out in an oil bath at 70 °C for 3 h under a nitrogen atmosphere. The resulting solution was purified by dialysis using a 12−14 kDa molecular weight cut off dialysis membrane against an excess amount of nanopure water (changed more than 3 times a day) for 4 days. The yield and concentration of HNPs was obtained by gravimetric analysis of lyophilized polymers. The hydrodynamic diameter of mHNPs was determined in 1X PBS at 25 °C using DLS equipped with Zetasizer Software (Zetasizer Nano ZS, Malvern Instruments Ltd., Worcestershire, U.K.).

Substrate Preparation. The Au substrates were coated by thermal vapor deposition of a 1 nm Cr adhesion layer and 45 nm Au onto Borosilicate No. 1.5 coverslips (Fisherbrand, Pittsburgh, PA). The Au surface was immobilized with 1-undecanethiol (C11) by immersing the Au substrate into a 1 mM C11/EtOH solution. The Au surface was partitioned using

DOI: 10.1021/acs.jpcc.6b05700
J. Phys. Chem. C 2016, 120, 16843−16849

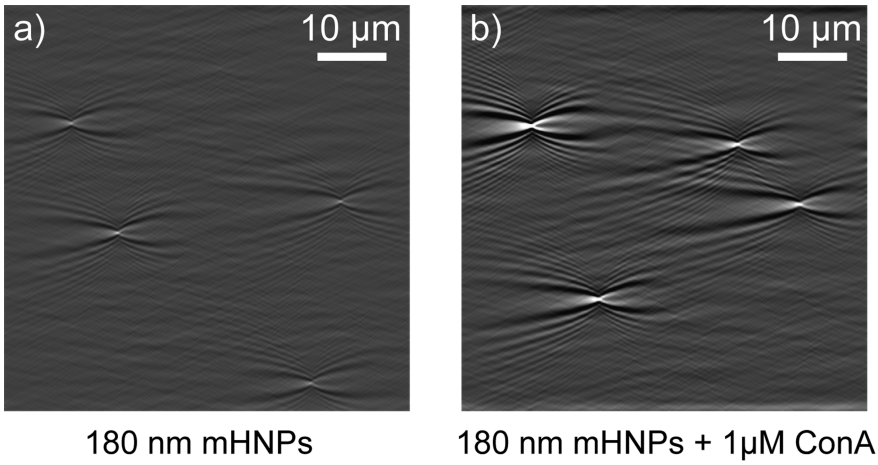

Figure 2. SPRI microscopy differential reflectivity images of (a) 180 nm mHNPs without Con A and (b) 180 nm mHNPs in the presence of 1 μM Con A. Each image is 58.5 μm × 58.5 μm.

adhesive silicone isolation wells (Electron Microscopy Sciences, Hafield, PA).

SPRI Microscopy Measurements. The SPRI microscope setup was described in a recent publication.[41] Briefly, the microscope was built into the frame of an IX51 inverted microscope (Olympus, Tokyo, Japan). A 1 mW near-infrared (814 nm) diode laser (Melles Griot, Carlsbad, CA) was expanded and collimated using a spatial filter (Newport Corp., Newport Beach, CA). The beam was polarized and then focused with a lens (f = 200 mm). The beam was directed onto the back focal plane of a 100× 1.49 high numerical aperture objective (Olympus) with a gold-coated knife-edge mirror (Thorlabs, Newton, NJ). The reflected image was passed to an Andor Neo sCMOS camera (South Windsor, CT). Each three-second reflectivity image was acquired by accumulating 30 11-bit, 0.1 s exposures.

Solutions of mHNPs were diluted in 1X PBS (11.9 mM phosphates, 13 mM sodium chloride, 2.7 mM potassium chloride, pH 7.4, Fisher) to concentrations specified in the experiments. Solutions of Concanavalin A (Sigma-Aldrich) were prepared in 1X PBS before mixing with mHNPs. SPRI microscopy experiments were performed after mixing mHNPs and Con A typically for 12 h at room temperature, though incubation times as short as 1 h worked equally well. For each experiment, 10 μL of mHNP solution was pipetted into the isolation well immediately preceding the image acquisition process.

RESULTS AND DISCUSSION

To quantitate the binding of the lectin Con A to hydrophobic mHNPs, real-time SPRI microscopy was used to characterize the irreversible adsorption of single mHNPs, in both the presence and absence of Con A, onto gold films functionalized with hydrophobic undecanethiol (C11) monolayers. In each SPRI adsorption measurement, SPRI microscopy reflectivity images were recorded every three seconds for a total time of 10 min, and then the images were sequentially subtracted from one another in order to obtain a series of differential reflectivity images. Figure 2 shows two typical SPRI microscopy differential reflectivity images that were obtained during the adsorption of mHNPs from different solutions: first, a solution of mHNPs (5 μg/mL) in the absence of Con A (Figure 2a), and second, a solution of mHNPs (5 μg/mL) in the presence of 1 μM Con A (Figure 2b). As demonstrated previously, the adsorption of a single mHNP appears in the SPRI microscopy differential reflectivity image as a point diffraction pattern. These patterns are due to the interaction of the mHNPs with the traveling surface plasmon polariton waves. Each image in Figure 2 shows four distinct point diffraction patterns (each spanning an area of at least 30 μm × 10 μm) that indicate the irreversible adsorption of four individual mHNPs onto the surface during these particular three-second time periods. As seen in Figure 2b, when Con A is present with the mHNPs, more intense point diffraction patterns are observed. We attribute this change in intensity to an increase in the refractive index of the mHNPs due to the various interactions (adsorption, uptake, and induced aggregation) of Con A with the mHNPs.

In order to quantify the observed increase in the individual mHNP point diffraction intensities in the presence of Con A, hundreds of point diffraction patterns from every SPRI adsorption measurement were analyzed. For every point diffraction pattern, the percent change in reflectivity, $\Delta\%R_{NP}$, was calculated from the region of maximum diffraction intensity in the image. We have used the same analysis method for calculating the $\Delta\%R_{NP}$ values as described in our previous publication.[30] Approximately 400 $\Delta\%R_{NP}$ values were obtained from each SPRI adsorption experiment (the cumulative number of adsorbed nanoparticles is plotted as a function of time for SPRI adsorption measurements at several mHNP concentrations in the Supporting Information). Figure 3 plots all of the individual $\Delta\%R_{NP}$ values measured during two different SPRI adsorption experiments: one experiment of mHNP without Con A (0 nM, open red circles) and the other experiment of mHNPs with 1 μM Con A (solid blue circles). It is readily apparent from the data in Figure 3 that the binding of Con A to mHNPs greatly increased the range of the individual $\Delta\%R_{NP}$ values; some point diffraction patterns had $\Delta\%R_{NP}$ values as large as 5%. In the absence of Con A, almost all of the $\Delta\%R_{NP}$ values were less than or equal to 1%. This increase in the range of $\Delta\%R_{NP}$ values can also be seen in Figure 4, which plots histograms representing the distribution of $\Delta\%R_{NP}$ values obtained in the presence of 0 nM, 100 nM, and 1 μM Con A. Additionally, the average $\Delta\%R_{NP}$ value for each experiment is plotted as a dotted black line in each histogram. This average $\Delta\%R_{NP}$, denoted as $\langle\Delta\%R_{NP}\rangle$, increased from a value of 0.51 ± 0.02% for mHNPs without Con A present to a value of 1.4 ±

DOI: 10.1021/acs.jpcc.6b05700
J. Phys. Chem. C 2016, 120, 16843−16849

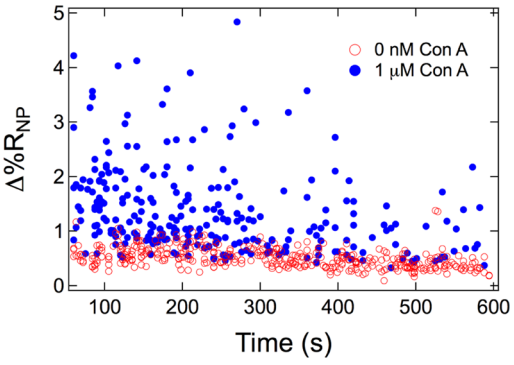

Figure 3. Time-dependent distribution of $\Delta\%R_{NP}$ values for mHNPs without Con A (0 nM, open red circles) and in the presence of 1 μM Con A (solid blue circles). Each circle represents the $\Delta\%R_{NP}$ for a single mHNP irreversibly adsorbing to the C11-functionalized surface.

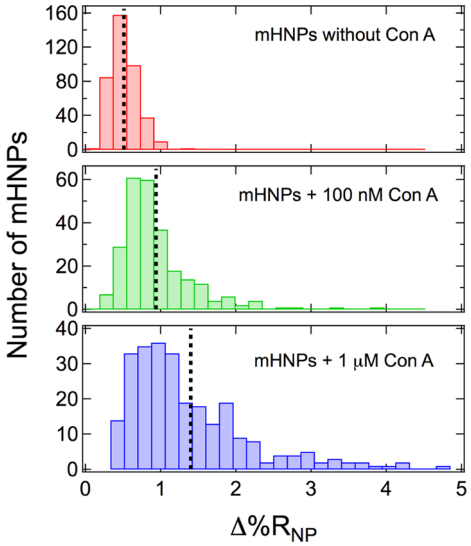

Figure 4. Distributions of $\Delta\%R_{NP}$ values for mHNPs mixed with no Con A (top), 100 nM Con A (middle), and 1 μM Con A (bottom), all plotted as histograms. The average $\Delta\%R_{NP}$ value for each experiment is plotted as a black dotted line in each histogram. For mHNPs mixed with no Con A, 100 nM Con A, and 1 μM Con A, average $\Delta\%R_{NP}$ values are 0.51 ± 0.02%, 0.94 ± 0.06%, and 1.4 ± 0.1%, respectively.

0.1% for mHNPs in the presence of 1 μM Con A. The error bars stated in this paper are the 95% confidence intervals, $\pm 2\sigma/(N)^{1/2}$, where σ is the standard deviation and N is the number of mHNPs measured in the SPRI microscopy experiment. A complete table of statistical data for these experiments is available in the Supporting Information. In order to confirm the specificity of the Con A binding to mHNPs, HNPs with no incorporated mannose units were mixed with Con A. No change in $\langle\Delta\%R_{NP}\rangle$ or the distribution of $\Delta\%R_{NP}$ values was found compared to HNPs in the absence of Con A (see Supporting Information).

The observed increase in $\langle\Delta\%R_{NP}\rangle$ in the presence of Con A is further examined in Figure 5, which plots the $\langle\Delta\%R_{NP}\rangle$ values as a function of Con A concentration. The $\langle\Delta\%R_{NP}\rangle$ values increase linearly from 0.51% to 1.4% at low Con A concentrations but then level off and do not change at concentrations above 200 nM. The highest concentration of Con A used in these experiments was 1 μM because Con A precipitated out of solution at concentrations above 1 μM.[46] We attribute this increase in $\langle\Delta\%R_{NP}\rangle$ to two effects: first, an

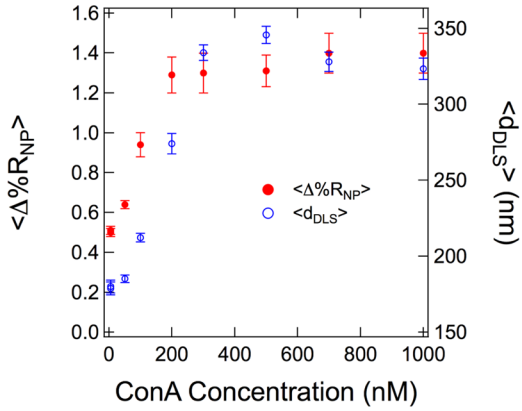

Figure 5. Average $\Delta\%R_{NP}$ values (solid red circles) from SPRI adsorption measurements and average hydrodynamic diameters (open blue circles) from DLS measurements for mHNPs mixed with varying concentrations of Con A, both plotted as a function of Con A concentration. Error bars are the 95% confidence intervals for the average $\Delta\%R_{NP}$ values and are the standard deviations for the average hydrodynamic diameters.

increase in the refractive index of the mHNPs due to the binding of Con A to the mannose in the mHNPs, and second, the specific aggregation of mHNPs induced by the presence of Con A. The lectin Con A contains four mannose binding sites, and thus mHNP aggregation can occur when Con A molecules that are attached to the outer portions of the mHNP cross-link by binding to more than one mHNP. The specific aggregation of sugar-modified nanoparticles due to Con A cross-linking has been reported previously.[47−49] In the presence of Con A, a Poisson distribution of the $\Delta\%R_{NP}$ values for individual mHNPs was not observed, further confirming that the changes in $\Delta\%R_{NP}$ values are due to a combination of both Con A binding to mHNPs and the specific Con A-induced aggregation. Above Con A concentrations of 200 nM, the observed leveling off of $\langle\Delta\%R_{NP}\rangle$ values is attributed to a saturation in both Con A binding and Con A-induced mHNP aggregation.

The measured increase of $\langle\Delta\%R_{NP}\rangle$ with Con A concentration can be compared with bulk DLS measurements in order to further characterize the Con A uptake process. The average hydrodynamic diameter of the nanoparticles, d_{DLS}, is also plotted as a function of Con A concentration in Figure 5 and is found to increase in a similar manner as $\langle\Delta\%R_{NP}\rangle$. This observation is different from the results reported previously for the study of melittin uptake into HNPs.[30] For those measurements, a linear increase in $\langle\Delta\%R_{NP}\rangle$ was observed for SPRI adsorption measurements in solutions with melittin concentrations between 0 μM and 2.5 μM, but no changes were observed in the d_{DLS}. In order to explain the data in Figure 5 for Con A binding to mHNPs, we conclude that the 104 kDa protein Con A, unlike the smaller peptide melittin, is unable to access the interior mannose groups of the hydrogel polymer and thus binds primarily to the outer regions of the mHNP. In addition, Con A can induce cross-linked aggregation by binding to mannose groups on more than one mHNP. Both the binding of Con A to the outer regions of the mHNPs and the specific aggregation of mHNPs induced by Con A cross-linking will lead to an increase in both $\langle\Delta\%R_{NP}\rangle$ and d_{DLS}.

Finally, in addition to changes in $\langle\Delta\%R_{NP}\rangle$ in the presence of Con A, the changes in the distribution of $\Delta\%R_{NP}$ values in the presence of Con A can be used to learn more about the lectin−

DOI: 10.1021/acs.jpcc.6b05700
J. Phys. Chem. C 2016, 120, 16843−16849

nanoparticle interactions. As seen in Figures 3 and 4, for mHNPs without Con A, the $\Delta\%R_{NP}$ values are tightly distributed in a range between 0.1 and 1.0%. However, this range of $\Delta\%R_{NP}$ values greatly expands in the presence of Con A, with $\Delta\%R_{NP}$ values as large as 5% at high Con A concentrations. In order to quantitate this expansion, we have arbitrarily divided the histogram distributions into the three subsets (labeled A, B, and C) as shown as an example in Figure 6a. These subsets include mHNPs with $\Delta\%R_{NP}$ values in the ranges of 0 to 1% (subset A), 1 to 2% (subset B), and above 2% (subset C). The fraction of mHNPs in each subset is plotted as a function of Con A concentration in Figure 6b. In the absence of Con A, nearly 100% of the mHNPs are in subset A ($\Delta\%R_{NP} \leq 1\%$). As Con A concentration increases, the number of mHNPs in subset A decreases, while the number of mHNPs in subsets B and C increases. The interaction of Con A with the mHNPs is strong: at a 200 nM Con A concentration, 60% of the mHNPs have a $\Delta\%R_{NP}$ value that is higher than the range of the values observed when no Con A was present (40% in subset B and 20% in subset C). Both the binding of multiple Con A molecules to mHNPs and the resulting specific aggregation of mHNPs substantially change the refractive index of individual mHNPs and thus the SPRI microscopy response. For example, the mHNPs in subset C have point diffraction intensities 6 to 10 times larger compared to the $\langle\Delta\%R_{NP}\rangle$ for mHNPs in the absence of Con A. These larger point diffraction intensities are most likely due to the adsorption of multiple aggregated mHNPs. Additionally, no changes in subset populations are seen at concentrations above 200 nM, suggesting that both the binding of Con A and the Con A-induced aggregation of mHNPs saturated at this point.

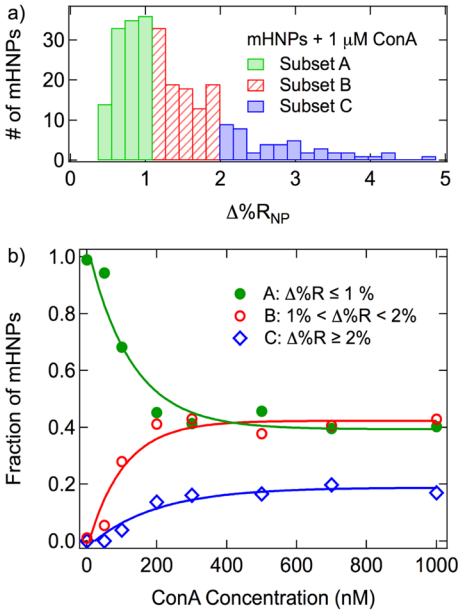

Figure 6. mHNPs were divided into three subsets based on their $\Delta\%R_{NP}$ values. (a) As an example, the histogram for mHNPs mixed with 1 μM Con A is shown again with the mHNPs divided into the three subsets. Subset A (green) contains all mHNPs with $\Delta\%R_{NP} \leq 1\%$; subset B (red) contains all mHNPs with $\Delta\%R_{NP}$ between 1 and 2%; and subset C (blue) contains all mHNPs with $\Delta\%R_{NP} \geq 2\%$. (b) The fraction of mHNPs in each subset is plotted as a function of Con A concentration. The saturation point for each curve is 200 nM.

CONCLUSIONS AND FUTURE DIRECTIONS

In this paper we have demonstrated how real-time single-nanoparticle SPRI microscopy can be used to characterize the binding of the lectin Con A to mannose-incorporated HNPs. By measuring both the average magnitude and distribution of the single point diffraction pattern intensities for mHNPs as a function of Con A concentration, we observed a significant binding of Con A to mHNPs that varied substantially from particle to particle. The SPRI microscopy data were used in conjunction with the observation of a concomitant increase in d_{DLS} as a function of Con A concentration. This allowed us to develop a model in which Con A protein primarily bound to the mannose units on the outer portions of the mHNPs and also induced aggregation of mHNPs by cross-linking with mannose units on multiple mHNPs. This Con A binding and mHNP aggregation process saturated at a Con A concentration of 200 nM. A large increase in the distribution of individual $\Delta\%R_{NP}$ values is observed and is attributed to a combination of mannose availability in mHNPs and Con A-induced aggregation of the mHNPs. Because the mHNPs both adsorb Con A and aggregate in its presence, the binding affinity between individual Con A molecules and mannose groups incorporated into the mHNPs cannot be determined from the SPRI data alone. In the future, we will apply our single-nanoparticle SPRI adsorption measurements to NIPAm-based HNPs that incorporate multiple types of sugar monomers in order to characterize the specificity, binding strength, and multivalency of other lectin−carbohydrate interactions.

ASSOCIATED CONTENT

Supporting Information

The Supporting Information is available free of charge on the ACS Publications website at DOI: 10.1021/acs.jpcc.6b05700.

Cumulative adsorption curves for SPRI adsorption measurements, statistical data for SPRI adsorption and DLS measurements, and mHNP control experiments (PDF)

AUTHOR INFORMATION

Corresponding Authors

*Robert M. Corn: rcorn@uci.edu.

*Yoshiko Miura: miuray@chem-eng.kyushu-u.ac.jp.

Author Contributions

§These authors contributed equally.

Notes

The authors declare no competing financial interest.

ACKNOWLEDGMENTS

This work was supported by the National Science Foundation through grants DMR-1308363 (KJS) and CHE-1403506 (RMC). DLS data were acquired at the Laser Spectroscopy Facility in the Department of Chemistry at UCI.

REFERENCES

(1) Hamidi, M.; Azadi, A.; Rafiei, P. Hydrogel Nanoparticles in Drug Delivery. *Adv. Drug Delivery Rev.* **2008**, *60*, 1638−1649.

(2) Peppas, N. A.; Hilt, J. Z.; Khademhosseini, A.; Langer, R. Hydrogels in Biology and Medicine: From Molecular Principles to Bionanotechnology. *Adv. Mater.* **2006**, *18*, 1345−1360.

(3) Nayak, S.; Lyon, L. A. Soft Nanotechnology with Soft Nanoparticles. *Angew. Chem., Int. Ed.* **2005**, *44*, 7686−7708.

DOI: 10.1021/acs.jpcc.6b05700
J. Phys. Chem. C 2016, 120, 16843−16849

(4) Seliktar, D. Designing Cell-Compatible Hydrogels for Biomedical Applications. *Science* **2012**, *336*, 1124−1128.
(5) Vermonden, T.; Censi, R.; Hennink, W. E. Hydrogels for Protein Delivery. *Chem. Rev.* **2012**, *112*, 2853−2888.
(6) Karimi, M.; Ghasemi, A.; Sahandi Zangabad, P.; Rahighi, R.; Moosavi Basri, S. M.; Mirshekari, H.; Amiri, M.; Shafaei Pishabad, Z.; Aslani, A.; Bozorgomid, M.; et al. Smart Micro/Nanoparticles in Stimulus-Responsive Drug/Gene Delivery Systems. *Chem. Soc. Rev.* **2016**, *45*, 1457−1501.
(7) Baeissa, A.; Dave, N.; Smith, B. D.; Liu, J. DNA-Functionalized Monolithic Hydrogels and Gold Nanoparticles for Colorimetric DNA Detection. *ACS Appl. Mater. Interfaces* **2010**, *2*, 3594−3600.
(8) Li, J.; Mo, L.; Lu, C. H.; Fu, T.; Yang, H. H.; Tan, W. Functional Nucleic Acid-Based Hydrogels for Bioanalytical and Biomedical Applications. *Chem. Soc. Rev.* **2016**, *45*, 1410−1431.
(9) Yonamine, Y.; Hoshino, Y.; Shea, K. J. ELISA-Mimic Screen for Synthetic Polymer Nanoparticles with High Affinity to Target Proteins. *Biomacromolecules* **2012**, *13*, 2952−2957.
(10) Lifson, M. A.; Carter, J. A.; Miller, B. L. Functionalized Polymer Microgel Particles Enable Customizable Production of Label-Free Sensor Arrays. *Anal. Chem.* **2015**, *87*, 7887−7893.
(11) Wang, Y. Z.; Li, D. Y.; He, X. W.; Li, W. Y.; Zhang, Y. K. Epitope Imprinted Polymer Nanoparticles Containing Fluorescent Quantum Dots for Specific Recognition of Human Serum Albumin. *Microchim. Acta* **2015**, *182*, 1465−1472.
(12) Yan, L.; Zhu, Z.; Zou, Y.; Huang, Y.; Liu, D.; Jia, S.; Xu, D.; Wu, M.; Zhou, Y.; Zhou, S.; et al. Target-Responsive "Sweet" Hydrogel with Glucometer Readout for Portable and Quantitative Detection of Non-Glucose Targets. *J. Am. Chem. Soc.* **2013**, *135*, 3748−3751.
(13) Zhao, H.; Jiang, G.; Weng, J.; Ma, Q.; Zhang, H.; Ito, Y.; Liu, M. A Signal-Accumulating DNAzyme-Crosslinked Hydrogel for Colorimetric Sensing of Hydrogen Peroxide. *J. Mater. Chem. B* **2016**, *4*, 4648−4651.
(14) Miura, Y. Synthesis and Biological Application of Glycopolymers. *J. Polym. Sci., Part A: Polym. Chem.* **2007**, *45*, 5031−5036.
(15) Bernard, J.; Hao, X.; Davis, T. P.; Barner-Kowollik, C.; Stenzel, M. H. Synthesis of Various Glycopolymer Architectures via RAFT Polymerization: From Block Copolymers to Stars. *Biomacromolecules* **2006**, *7*, 232−238.
(16) Ghadban, A.; Albertin, L. Synthesis of Glycopolymer Architectures by Reversible-Deactivation Radical Polymerization. *Polymers* **2013**, *5*, 431−526.
(17) Chen, Y.; Espeel, P.; Reinicke, S.; Du Prez, F. E.; Stenzel, M. H. Control of Glycopolymer Nanoparticle Morphology by a One-Pot, Double Modification Procedure Using Thiolactones. *Macromol. Rapid Commun.* **2014**, *35*, 1128−1134.
(18) Zhang, Q.; Collins, J.; Anastasaki, A.; Wallis, R.; Mitchell, D. A.; Becer, C. R.; Haddleton, D. M. Sequence-Controlled Multi-Block Glycopolymers to Inhibit DC-SIGN-gp120 Binding. *Angew. Chem., Int. Ed.* **2013**, *52*, 4435−4439.
(19) Gou, Y.; Geng, J.; Richards, S. J.; Burns, J.; Remzi Becer, C.; Haddleton, D. M. A Detailed Study on Understanding Glycopolymer Library and Con A Interactions. *J. Polym. Sci., Part A: Polym. Chem.* **2013**, *51*, 2588−2597.
(20) Yilmaz, G.; Becer, C. R. Precision Glycopolymers and Their Interactions with Lectins. *Eur. Polym. J.* **2013**, *49*, 3046−3051.
(21) Su, S.; Wang, H.; Liu, X.; Wu, Y.; Nie, G. iRGD-Coupled Responsive Fluorescent Nanogel for Targeted Drug Delivery. *Biomaterials* **2013**, *34*, 3523−3533.
(22) Wolfbeis, O. S. An Overview of Nanoparticles Commonly Used in Fluorescent Bioimaging. *Chem. Soc. Rev.* **2015**, *44*, 4743−4768.
(23) De Koker, S.; Cui, J.; Vanparijs, N.; Albertazzi, L.; Grooten, J.; Caruso, F.; De Geest, B. G. Engineering Polymer Hydrogel Nanoparticles for Lymph Node-Targeted Delivery. *Angew. Chem., Int. Ed.* **2016**, *55*, 1334−1339.
(24) Hoshino, Y.; Nakamoto, M.; Miura, Y. Control of Protein-Binding Kinetics on Synthetic Polymer Nanoparticles by Tuning Flexibility and Inducing Conformation Changes of Polymer Chains. *J. Am. Chem. Soc.* **2012**, *134*, 15209−15212.
(25) Cho, E. J.; Holback, H.; Liu, K. C.; Abouelmagd, S. A.; Park, J.; Yeo, Y. Nanoparticle Characterization: State of the Art, Challenges, and Emerging Technologies. *Mol. Pharmaceutics* **2013**, *10*, 2093−2110.
(26) Smith, M. H.; Lyon, L. A. Tunable Encapsulation of Proteins within Charged Microgels. *Macromolecules* **2011**, *44*, 8154−8160.
(27) Ballauff, M.; Lu, Y. "Smart" Nanoparticles: Preparation, Characterization and Applications. *Polymer* **2007**, *48*, 1815−1823.
(28) Karg, M.; Hellweg, T. New "Smart" poly(NIPAM) Microgels and Nanoparticle Microgel Hybrids: Properties and Advances in Characterisation. *Curr. Opin. Colloid Interface Sci.* **2009**, *14*, 438−450.
(29) Yaghmur, A.; Helvig, S.; Azmi, I.; Moghimi, S. Recent Advances in Cryo-TEM Imaging of Soft Lipid Nanoparticles. *AIMS Biophysics* **2015**, *2*, 116−130.
(30) Cho, K.; Fasoli, J. B.; Yoshimatsu, K.; Shea, K. J.; Corn, R. M. Measuring Melittin Uptake into Hydrogel Nanoparticles with Near-Infrared Single Nanoparticle Surface Plasmon Resonance Microscopy. *Anal. Chem.* **2015**, *87*, 4973−4979.
(31) Rothenhäusler, B.; Knoll, W. Surface-Plasmon Microscopy. *Nature* **1988**, *332*, 615−617.
(32) Zybin, A.; Kuritsyn, Y. A.; Gurevich, E. L.; Temchura, V. V.; Überla, K.; Niemax, K. Real-time Detection of Single Immobilized Nanoparticles by Surface Plasmon Resonance Imaging. *Plasmonics* **2010**, *5*, 31−35.
(33) Weichert, F.; Gaspar, M.; Timm, C.; Zybin, A.; Gurevich, E. L.; Engel, M.; Müller, H.; Marwedel, P. Signal Analysis and Classification for Surface Plasmon Assisted Microscopy of Nanoobjects. *Sens. Actuators, B* **2010**, *151*, 281−290.
(34) Giebel, K. F.; Bechinger, C.; Herminghaus, S.; Riedel, M.; Leiderer, P.; Weiland, U.; Bastmeyer, M. Imaging of Cell/Substrate Contacts of Living Cells with Surface Plasmon Resonance Microscopy. *Biophys. J.* **1999**, *76*, 509−516.
(35) Jamil, M. M.; Denyer, M. C.; Youseffi, M.; Britland, S. T.; Liu, S.; See, C. W.; Somekh, M. G.; Zhang, J. Imaging of the Cell Surface Interface Using Objective Coupled Widefield Surface Plasmon Microscopy. *J. Struct. Biol.* **2008**, *164*, 75−80.
(36) Wang, S.; Shan, X.; Patel, U.; Huang, X.; Lu, J.; Li, J.; Tao, N. Label-Free Imaging, Detection, and Mass Measurement of Single Viruses by Surface Plasmon Resonance. *Proc. Natl. Acad. Sci. U. S. A.* **2010**, *107*, 16028−16032.
(37) Gurevich, E. L.; Temchura, V. V.; Überla, K.; Zybin, A. Analytical Features of Particle Counting Sensor Based on Plasmon Assisted Microscopy of Nano Objects. *Sens. Actuators, B* **2011**, *160*, 1210−1215.
(38) Wang, W.; Foley, K.; Shan, X.; Wang, S.; Eaton, S.; Nagaraj, V. J.; Wiktor, P.; Patel, U.; Tao, N. Single Cells and Intracellular Processes Studied by a Plasmonic-Based Electrochemical Impedance Microscopy. *Nat. Chem.* **2011**, *3*, 251−257.
(39) Wang, W.; Wang, S.; Liu, Q.; Wu, J.; Tao, N. Mapping Single-Cell-Substrate Interactions by Surface Plasmon Resonance Microscopy. *Langmuir* **2012**, *28*, 13373−13379.
(40) Wang, W.; Tao, N. Detection, Counting, and Imaging of Single Nanoparticles. *Anal. Chem.* **2014**, *86*, 2−14.
(41) Halpern, A. R.; Wood, J. B.; Wang, Y.; Corn, R. M. Single-Nanoparticle Near-Infrared Surface Plasmon Resonance Microscopy for Real-Time Measurements of DNA Hybridization Adsorption. *ACS Nano* **2014**, *8*, 1022−1030.
(42) Yang, Y.; Yu, H.; Shan, X.; Wang, W.; Liu, X.; Wang, S.; Tao, N. Label-Free Tracking of Single Organelle Transportation in Cells with Nanometer Precision Using a Plasmonic Imaging Technique. *Small* **2015**, *11*, 2878−2884.
(43) Toyoshima, M.; Miura, Y. Preparation of Glycopolymer-Substituted Gold Nanoparticles and Their Molecular Recognition. *J. Polym. Sci., Part A: Polym. Chem.* **2009**, *47*, 1412−1421.
(44) Terada, Y.; Hashimoto, W.; Endo, T.; Seto, H.; Murakami, T.; Hisamoto, H.; Hoshino, Y.; Miura, Y. Signal Amplified Two-Dimensional Photonic Crystal Biosensor Immobilized with Glyco-Nanoparticles. *J. Mater. Chem. B* **2014**, *2*, 3324−3332.

DOI: 10.1021/acs.jpcc.6b05700
J. Phys. Chem. C 2016, 120, 16843−16849

(45) Debord, J. D.; Lyon, L. A. Synthesis and Characterization of pH-Responsive Copolymer Microgels with Tunable Volume Phase Transition Temperatures. *Langmuir* **2003**, *19*, 7662−7664.
(46) Ding, L.; Qian, R.; Xue, Y.; Cheng, W.; Ju, H. In Situ Scanometric Assay of Cell Surface Carbohydrate by Glyconanoparticle-Aggregation-Regulated Silver Enhancement. *Anal. Chem.* **2010**, *82*, 5804−5809.
(47) Hone, D. C.; Haines, A. H.; Russell, D. A. Rapid, Quantitative Colorimetric Detection of a Lectin Using Mannose-Stabilized Gold Nanoparticles. *Langmuir* **2003**, *19*, 7141−7144.
(48) Schofield, C. L.; Haines, A. H.; Field, R. A.; Russell, D. A. Silver and Gold Glyconanoparticles for Colorimetric Bioassays. *Langmuir* **2006**, *22*, 6707−6711.
(49) Kober, M.; Moros, M.; Franco Fraguas, L.; Grazu, V.; de la Fuente, J. M.; Luna, M.; Briones, F. Nanoparticle-Mediated Monitoring of Carbohydrate-Lectin Interactions Using Transient Magnetic Birefringence. *Anal. Chem.* **2014**, *86*, 12159−12165.

DOI: 10.1021/acs.jpcc.6b05700
J. Phys. Chem. C 2016, 120, 16843−16849